Solvent-Driven Gate Opening in MOF-76-Ce: Effect on CO2 Adsorption

CHEMISTRY & SUSTAINABILITY
CHEMSUSCHEM
ENERGY & MATERIALS

Supporting Information

Solvent-Driven Gate Opening in MOF-76-Ce: Effect on CO_2 Adsorption

Jayashree Ethiraj,[a] Francesca Bonino,*[a] Jenny G. Vitillo,[a, b] Kirill A. Lomachenko,[a, c] Carlo Lamberti,[c, d] Helge Reinsch,[e] Karl Petter Lillerud,[e] and Silvia Bordiga[a]

cssc_201501574_sm_miscellaneous_information.pdf

Supporting Information

S1. Scanning Electron Microscopy

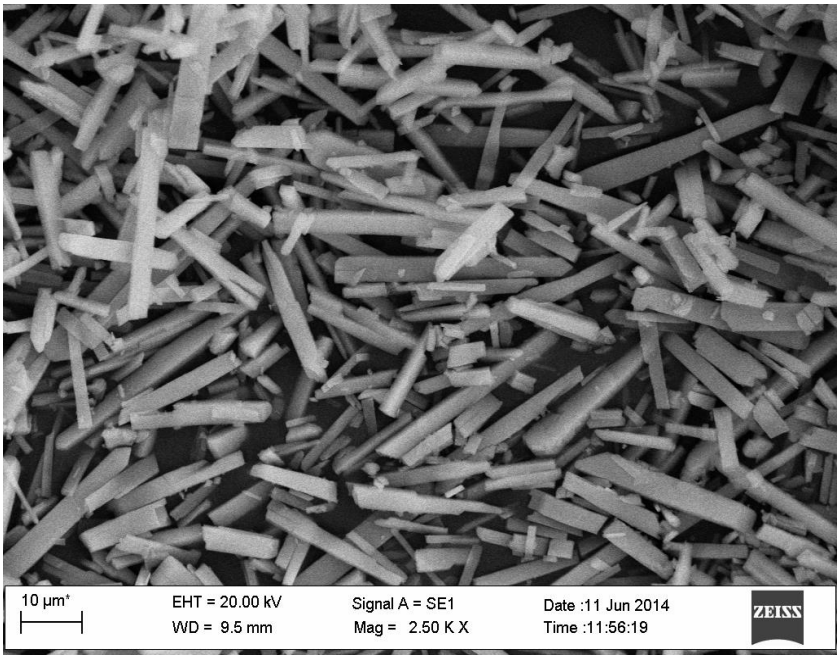

Figure S1. SEM image of $[Ce(BTC)(H_2O)].H_2O_nDMF_n$.

Electron microscopy images were obtained by means of a Scanning Electron Microscope (SEM) EVO 50XVP Carl Zeiss AG (20 kV acceleration potential). Secondary electrons were used for getting images.

The SEM image of $[Ce(BTC)(H_2O)].H_2O_nDMF_n$ shows very well dispersed needle shape crystals with average length of nearly 20 μm.

S2 Thermogravimetric Analysis

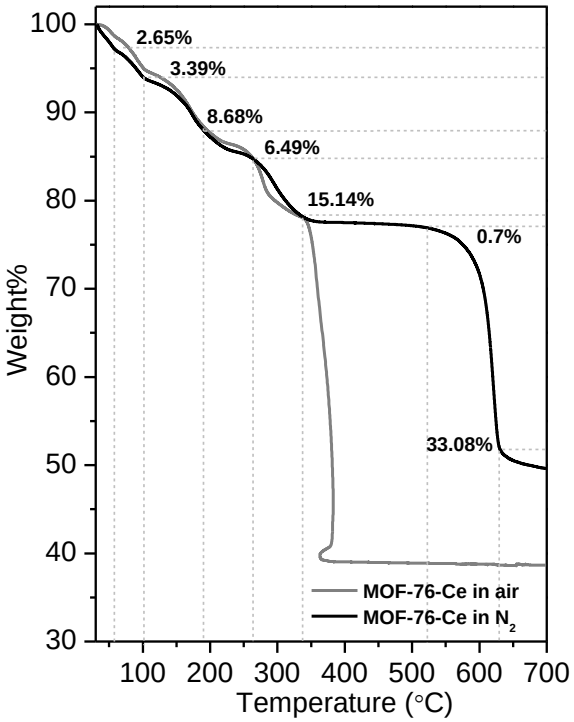

Figure S2. TGA curves of as-synthesized $[Ce(BTC)]H_2O_nDMF_m$ in N_2 and in air flow.

Thermal gravimetric analysis (TGA) was carried out on a TAQ600 (TA Instruments) with the heating rate of 3°C/min from RT to 700°C in a nitrogen flow. Before starting the measurements, the samples were flushed in N_2 at RT and equilibrated at 30°C for 30mins. The procedure was repeated in air flow.

The TGA curves reported in Figure S2 show the wt% loss of MOF-76-Ce in N_2 and in air flow vs. temperature. Channel water loss is probably observed in two steps till 100°C. DMF loss occurs probably in various steps. However weight loss couldn't be precisely associated to molecules lost as there is structural transformation occuring from 25°C to 250°C (see Figure 1 in the main text). In the case of N_2 flow, the 350°C -525°C plateau region shows no loss of organic linker. A rapid loss of nearly 33% is seen in the temperature range 525-625°C, showing loss of organic linker. At

700°C there is formation of coke and CeO_2. In case of air flow, it seems that already at 350°C the MOF is decomposed in CeO_2, H_2O and CO_2.

S3 Raman Spectroscopy

Raman spectra were recorded on a Renishaw inVia Raman microscope spectrometer equipped with a diode laser emitting at 785 nm. Photons scattered by the sample were dispersed by a 1200 lines/mm grating monochromator and were simultaneously collected on a CCD camera; the collection optic was 20X objective. The spectral collection setup consisted of 50 acquisitions, each of 10 s at 5% of laser power.

Figure S3a shows well synthesized MOF-76-Ce in comparison with HKUST-1 ($Cu_3(BTC)_2$), since the linker is BTC in both MOF-76-Ce and HKUST-1.[1] The vibrational fingerprints of the carboxylate groups should be conserved in the two MOFs and this is clearly seen. The comparison with the precursors namely $Ce(NO_3)_3{\cdot}6H_2O$ and H_3BTC clearly shows the formation of MOF-76-Ce as most of the precursor vibrational modes are not visible in the synthesized MOF. Figure S3b shows Raman Spectra of MOF-76-Ce in air (**MOF-76-Ce-fs**) and upon activation in vacuum at 250°C for 2 h (**MOF-76-Ce-ds**). DMF is removed upon activation and there are small shifts seen in $\nu_{asym}(COO^-)$ and $\nu_{sym}(COO^-)$ modes (1700-1400 cm^{-1} range). A small shift of the band at 402 cm^{-1} (now at 410 cm^{-1}) is also observed. This feature could be assigned to a vibrational mode deeply involving a Ce-O bond.

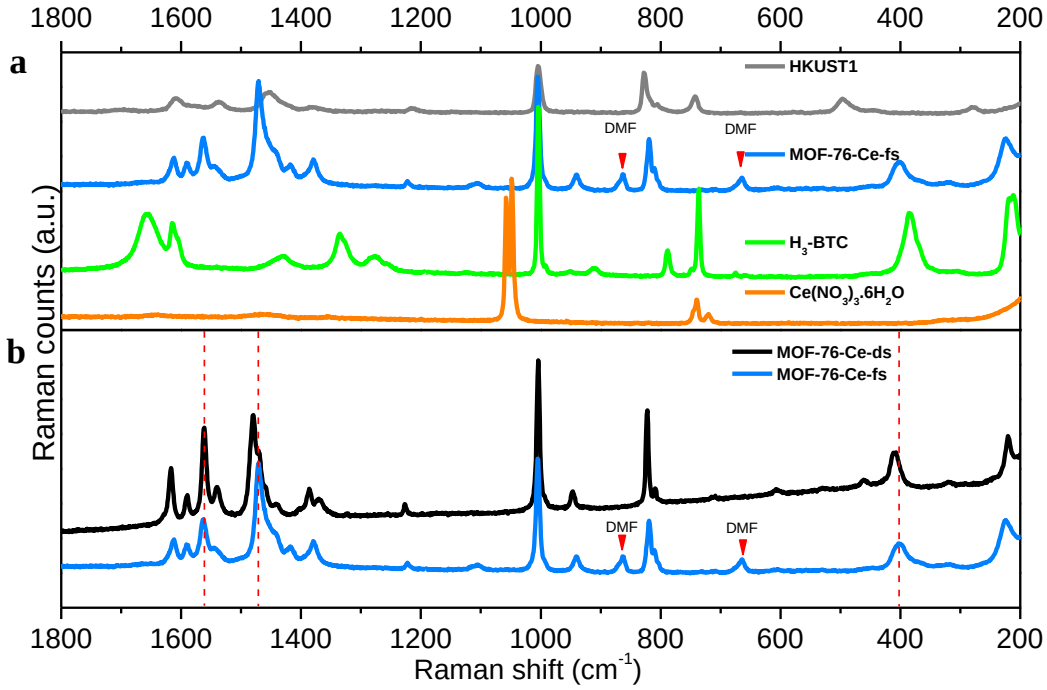

Figure S3. a) Raman spectra of precursors, $Ce(NO_3)_3.6H_2O$ (orange), H_3BTC(green) and of **MOF-76-Ce** (light blue) and $Cu_3(BTC)_2$ (grey) MOFs in air. b) Comparison of solvated **MOF-76-Ce** in air (**MOF-76-Ce-fs**, light blue) and fully desolvated (**MOF-76-Ce-ds**, black).

S4 High Resolution Powder X-ray Diffraction and Rietveld refinement

The pattern measured under ambient conditions showed very strong similarities with a simulated pattern of MOF-76. Therefore the crystal structure of this compound was used as a starting point for Rietveld refinement. It is worth mentioning that the reported space group for MOF-76 ($P4_322$) is indistinguishable from its analogue ($P4_122$) by PXRD methods and therefore it was assumed that the reported compound crystallizes in both enantiomorphic space groups. The refinement confirmed the assumption that **MOF-76-Ce** material, in its fully solvated form (at 25°C, **MOF-76-Ce-fs**), is a MOF-76 analogue. However, tiny amounts of a crystalline impurity were observed, as indicated by peaks of very weak intensity which do not match with the refined structure (Figure S3). Successively, a structural model of the half solvated sample (at 180°C, **MOF-76-Ce-hs)** was developed. The majority of peaks matches well with an orthorhombic unit cell (space group $C222_1$) with cell parameters a = 17.201(3) Å, b = 11.615(2) Å and c = 13.450(2) Å as determined by indexing. This space group represents a translationengleiche subgroup of $P4_322$. Thus the refined structure in $P4_322$ was converted to a hypothetical structure in $C222_1$ using PowderCell, resulting in changed cell parameters of a = 14.8331 Å, b = 14.8331 Å and c = 14.2615 Å. This hypothetical structure was further manipulated using Materials Studio.[2] The cell parameters were changed to the indexed values and the structure was optimized by means of force-field calculations. The thus obtained structural model was refined by Rietveld methods. It turned out that one half of the solvent molecules coordinated to Ce-ions in the *as*-structure was removed at this stage while the other half remained coordinated, resulting as well in a contraction of the square-shaped channels to rather rhombic shape (see Figure 2). A third pattern measured at 350°C (**MOF-76-Ce-ds**, see Figure S3c) indicated reconstruction of the tetragonal symmetry, although small amounts of the intermediate are still present. The crystal structure of the as-synthesized material was used as starting point for the Rietveld refinement. After converging, it was observed that all solvent molecules were removed at this temperature and the tetragonal symmetry is restored while the coordination environment of the Ce ions is changed due to the complete removal of coordinated solvent (Figure 2). Table 1

summarises the results obtained from the Rietvel refinement for **MOF-76-Ce-fs, MOF-76-Ce-hs** and **MOF-76-Ce-ds**. For the refinement of the room temperature structure the electron density inside the pores of the MOF was modeled by partially occupied oxygen atoms which serve as placeholders for occluded guest molecules and all other atoms were freely refined. The further high resolution patterns were collected at 180°C under a flow of nitrogen and at 350°C which show stable structures and the maximum conversion to the respective structures under these experimental conditions (capillary and N_2 atmosphere). While the structure of the compounds observed at room temperature could be freely refined, at elevated temperatures the benzene rings of the linker molecules had to be treated as rigid bodies (at 180°C) or constrained at their position (at 350°C). For the pattern measured at 350°C the ranges where peaks of the intermediate structure were present were excluded from the refinement.

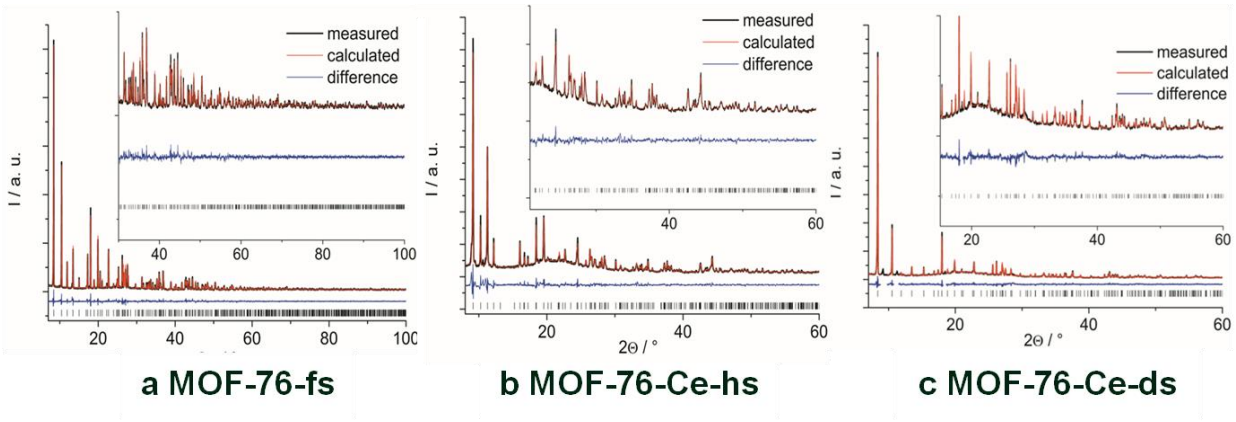

Figure S4. Rietveld plots for the compound at (from top to bottom) 25°C (**MOF-76-Ce-fs**), 180°C (**MOF-76-Ce-hs**) and 350°C (**MOF-76-Ce-ds**). The black curves give the experimental data, the red curves give the calculated patterns and the blue curves mark the differences. The vertical bars mark the Bragg-reflection position. In the case of the refinement at 350°C, the regions where peaks of the intermediate are present could be excluded from the refinement. Accordingly the symmetry along the inorganic chains is lowered from 4_3-axes to 2_1-axes.

Table S1. Some relevant parameters of the Rietveld refinements of the patterns collected on the three different MOF-76-Ce-samples.

Crystallographic parameters	**MOF-76-Ce-fs**	**MOF-76-Ce-hs**	**MOF-76-Ce-ds**
space group	$P4_322$	$C222_1$	$P4_322$
a / Å	10.4886(1)	17.2103(6)	10.5297(2)
b / Å	10.4886(1)	11.6251(5)	10.5297(2)
c / Å	14.2615(2)	13.4592(5)	13.8829(4)
$\alpha = \beta = \gamma$ / °	90	90	90
V / Å^3	1568.91(3)	2692.8(2)	1539.26(6)
R_{WP}/%	9.0	7.9	8.0
R_{Bragg}/%	2.7	2.1	2.9
GoF	1.8	2.0	1.4

S5 Comparison of PXRD of MOF76-Ce treated in vacuum and in flow.

Powder patterns from samples used for structure refinement and adsorption measurements, (N_2 flow or vacuum and slightly different temperatures respectively) were compared in order to verify that the structure under investigation are comparable. Figure S5 clearly shows how treatment in vacuum at 25, 150, 250°C and in N_2 flow at 25, 180, 350°C gave rise to the same sample structure, namely: **MOF76-Ce -fs**, **MOF76-Ce hs**, **MOF76-Ce-ds**.

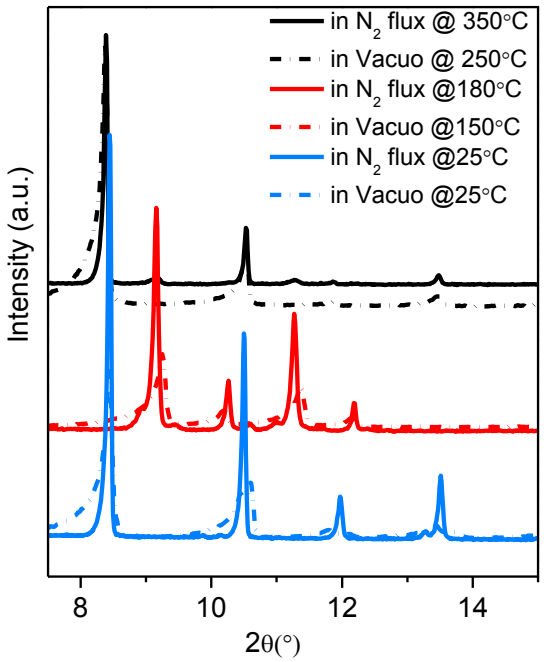

Figure S5. Comparison of PXRD of Ce-BTC treated in vacuum at 25, 150, 250°C and in N_2 flow at 25, 180, 350°C, respectively, **MOF76-Ce-fs**, **MOF76-Ce -hs**, **MOF76-Ce -ds**.

S6 EXAFS: evolution of local environment of Ce species upon activation

As evidenced by the experimental EXAFS data, presented in Figure S6a, major changes in Ce local environment occur in the temperature range of 60-120°C. They coincide with the release of solvent (H_2O and DMF, being water most prominent at temperature below 100°C, see Figure S6b). Most pronounced changes are in the nearest coordination shells (i.e. nine oxygen and two carbon atoms), since the intensity of the corresponding EXAFS peak goes down dramatically. After 120°C virtually no change happens to the sample, as far as Ce local environment is concerned. Gradual decrease of the first EXAFS peak upon heating from 120°C up to 350°C is due to a temperature-related rise of Debye-Waller factor, which is confirmed by the restoration of the peak intensity upon cooling of the activated material down to 30°C. Indeed, in the final "activated" state the intensity is virtually the same as for the 77-120°C spectrum.

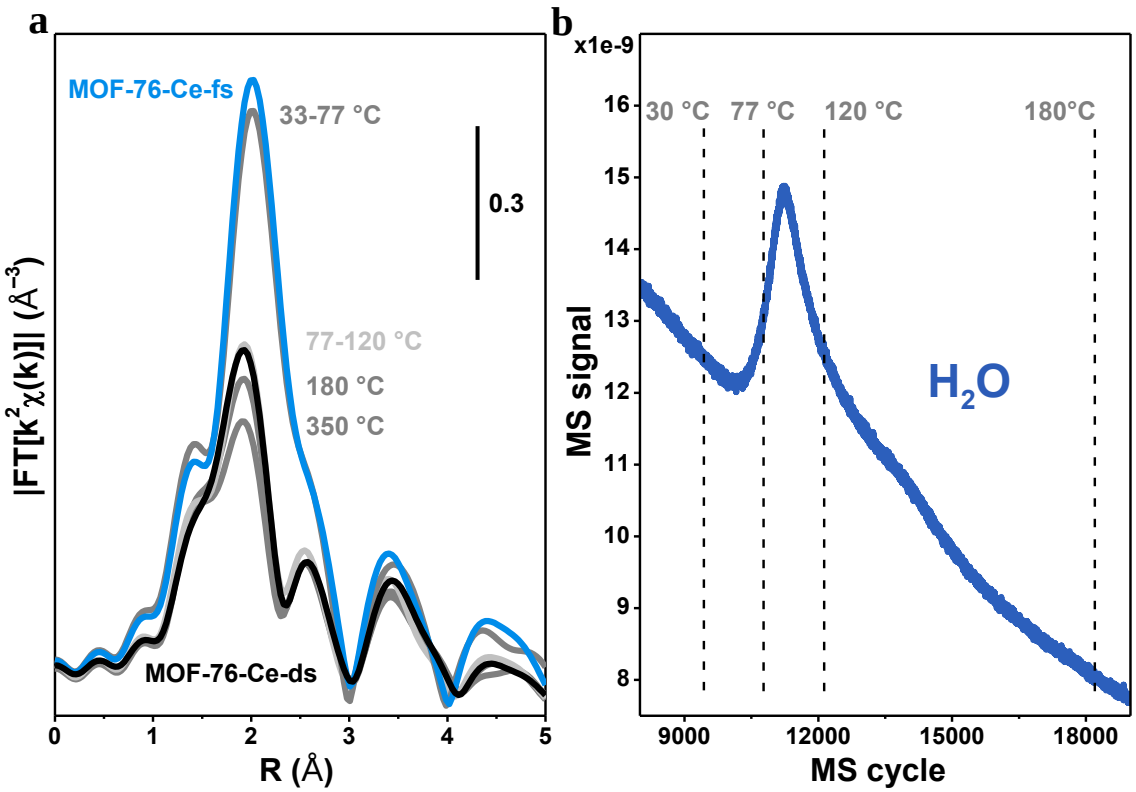

Figure S6. a) Fourier-transform modulus of phase-uncorrected experimental k^2-weighted EXAFS signal of **MOF-76-Ce** MOF. **MOF-76-Ce-fs** spectrum (light blue line) is collected at 25°C, **MOF-76-Ce-ds** (black line) at 30°C after activating the materials by heating up to 350°C and cooling

down, always in He flow. Grey lines with indicated temperatures represent different intermediate states on the heating ramp. Spectrum taken between 77 and 120°C is highlighted in black in order to demonstrate the similarity with the "activated" datum. b) Mass spectrometer water signal during the activation. Dashed lines indicate the temperature of the sample.

S7 EXAFS: fitting details

EXAFS spectra of solvated and activated material were fitted using the corresponding PXRD geometries as models for calculation of phase shifts and scattering amplitudes. The model for the solvated sample (**MOF-76-Ce-fs**) is presented in the Figure 3b.

Parameterization of EXAFS fit for **MOF-76-Ce-fs** was performed as follows. Single scattering paths formed by the atoms nearest to Ce (those with halos in Figure 3b) were given a unique expansion factor α, so the bond length between Ce and an atom n was expressed as

$$R_n = (1 + \alpha) \cdot R_n^{PXRD}, \quad (1)$$

where $R_n^{PXRD}$is an effective path length for the atom n determined by PXRD. For single scattering paths, it is equal to the bond length. Debye-Waller (DW) factors for these paths were obtained fitting a unique parameter σ^2. The DW factor of each path was expressed as

$$\sigma_n^2 = \sigma^2 \cdot \sqrt{\frac{R_n^{PXRD}}{R_{O1}^{PXRD}}}, \quad (2)$$

where $R_{O1}^{PXRD}$is an effective path length for the atom *O1* determined by PXRD. In addition, amplitude reduction factor and energy shift were included in the fit, the same for all the paths. They are denoted respectively S_0^2 and ΔE in Table S2.

Since the k-range of the analysed data is very short due to the intrinsic limitation, that is the presence of Ce L_2 edge, the peaks in the EXAFS FT are very broad. Therefore, a tail from the distant shells contributes significantly to the intensity at the low-R region as well. In order to account for this effect, single and multiple scattering paths with effective length up to 5 Å were

included in the calculation of EXAFS. The atoms that form these paths are shown in Figure 3b without halos. However, it was not possible to fit their distances reliably due to the complexity of the structure and, most of all, because of the limited range of the experimental data. Thus, their distances were fixed and a progressively increasing DW factor was assigned for each of these paths as follows:

$$\sigma_n^2 = \sigma_0^2 \cdot \sqrt{\frac{R_n^{PXRD}}{R_0}}, \quad (3)$$

where $\sigma_0^2 = 0.008$ Å^{-2} and $R_0 = 3.39$ Å are respectively the DW factor and the effective length of the shortest path of this group. In this way, taking account these paths to simulate a "background" for the peak formed by the nearest shells did not increase the number of free parameters in the fit. This approach is typical for data collection in short k-region for well-ordered materials. [3]

Parameterization of the activated model (**MOF-76-Ce-ds**) was done in the same way, starting from the corresponding PXRD model. The only differences were the S_0^2 parameter that was fixed to the value of 1.22, obtained for the **MOF-76-Ce-fs** spectrum, and the value of $R_0 = 3.45$ Å used in the expression (3). Such high value of S_0^2 (which in principle should not be more than 1) is explained by high degree of correlation with σ^2, which is also quite elevated. Fixing S_0^2 to 1 leads to the decrease of σ^2, but does not alter the best-fit values of structural parameters. Values for the best-fit parameters and other data related to the fits are presented in Table S2.

Table S2. Best fit EXAFS parameters for **MOF-76-Ce-fs** and **MOF-76-Ce-ds** samples

Parameter	**MOF-76-Ce-fs**	**MOF-76-Ce-ds**
Fitting range in k, Å^{-1}	2.74 – 9.87	
Fitting range in R, Å	1.55 – 3.00	
Number of independent points	6.38	
Number of fitting parameters	4	3

S_0^2	1.22 ± 0.06	1.22*
ΔE, eV	6.6 ± 0.4	7.9 ± 1.3
α	0.030 ± 0.002	0.010 ± 0.006
σ^2 , $Å^2$	0.0067 ± 0.0009	0.007 ± 0.001
R-factor	0.001	0.028

(*) fixed at the value obtained for the **MOF-76-Cefs** model**.**

Table S3 represents the values for bond distances and DW factors for the nearest Ce shells in the EXAFS best-fit configurations compared to PXRD data. The EXAFS values and the corresponding errors were obtained from the best-fit α and σ^2 parameters using the formulas (1) and (2).

Table S3. Structural parameters for the EXAFS best fit models compared to PXRD data

Path	Parameter	MOF-76-Ce-fs EXAFS	MOF-76-Ce-fs PXRD	MOF-76-Ce-ds EXAFS	MOF-76-Ce-ds PXRD
O1	R, Å	2.46 ± 0.01	2.39	2.41 ± 0.01	2.38
	σ^2 , $Å^2$	0.007 ± 0.001	-	0.007 ± 0.001	-
O2	R, Å	2.50 ± 0.01	2.43	2.48 ± 0.01	2.46
	σ^2 , $Å^2$	0.007 ± 0.001	-	0.007 ± 0.001	-
O3	R, Å	2.55 ± 0.01	2.48	2.75 ± 0.02	2.72
	σ^2 , $Å^2$	0.007 ± 0.001	-	0.008 ± 0.001	-
Osol	R, Å	2.62 ± 0.01	2.55	-	-
	σ^2 , $Å^2$	0.007 ± 0.001	-	-	-
C1	R, Å	3.14 ± 0.01	3.04	3.04 ± 0.02	3.01
	σ^2 , $Å^2$	0.008 ± 0.001	-	0.008 ± 0.001	-
O4	R, Å	3.18 ± 0.01	3.09	3.14 ± 0.02	3.11
	σ^2 , $Å^2$	0.008 ± 0.001	-	0.008 ± 0.001	-

S8 N_2 adsorption isotherms

Surface area analysis was performed at four activation temperatures, 150, 250, 350 and 450°C in dynamic vacuum (see Figure S7 and Table S2). On the sample activated at 150°C no significant N_2 adsorption was obtained, indicating as the pores of the material are not accessible to N_2. Upon activation at 250°C very high N_2 adsorption values were obtained. Further increasing in activation temperature to 350°C and 450°C resulted in two almost coincident isotherms, giving only slightly lower adsorption values. This is a further proof of the high thermal stability of the material. The main observation from surface area analysis shows that the structural transition occuring at 150°C (**MOF-76-Ce-hs** structure) does not allow the N_2 molecules to enter the pores, which become accessible only when the next transition happens in agreement with theoretical simualtions. The activation temperature is then a key factor for the opening of the pores, which acts as a gate for N_2 molecule.

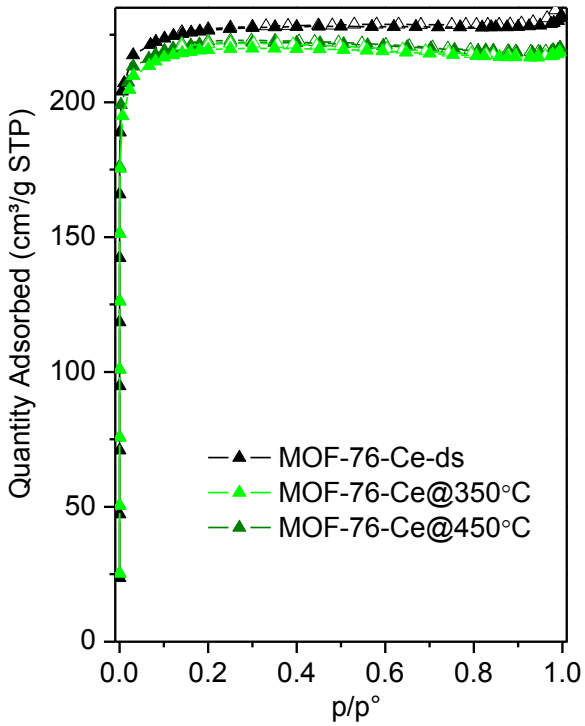

Figure S7. Volumetric N_2 adsorption isotherms recorded at -196°C on **MOF-76-Ce** activated at 250°C (**MOF-76-Ce-ds**), 350°C and 450°C. Filled and empty scatters refer to the adsorption and desorption branches.

For sake of completeness, an evaluation of Surface Area was performed with MATERIAL STUDIO. These calculations showed that **MOF-76-Ce-hs** is hardly accessible for molecules with the size of nitrogen. The diameter of the channels is very close to the diameter of nitrogen molecules. Thus the experimental inaccessibility of the channels for nitrogen is highly plausible since the diffusion into these narrow channels is substantially impeded. The expected surface area for the fully desolvated form ranges from 792 m^2/g to 840 m^2/g, depending on the molecular probe diameter. This is in reasonable agreement with the experimentally obtained values (Table 1 and Table S4).

S9-Volumetric CO_2 isotherms

For the sake of completeness, volumetric CO_2 isotherms measured on Ce-BTC sample activated at 350°C and 450°C are also reported (see Figure S8). They are almost coincident and placed in the middle of those ones obtained on the sample activated at 150°C (**MOF-76-Ce-hs**) and 250°C (**MOF-76-Ce-ds**). Table S4 reports the complete set of values for CO_2 storage capacity at the different temperatures.

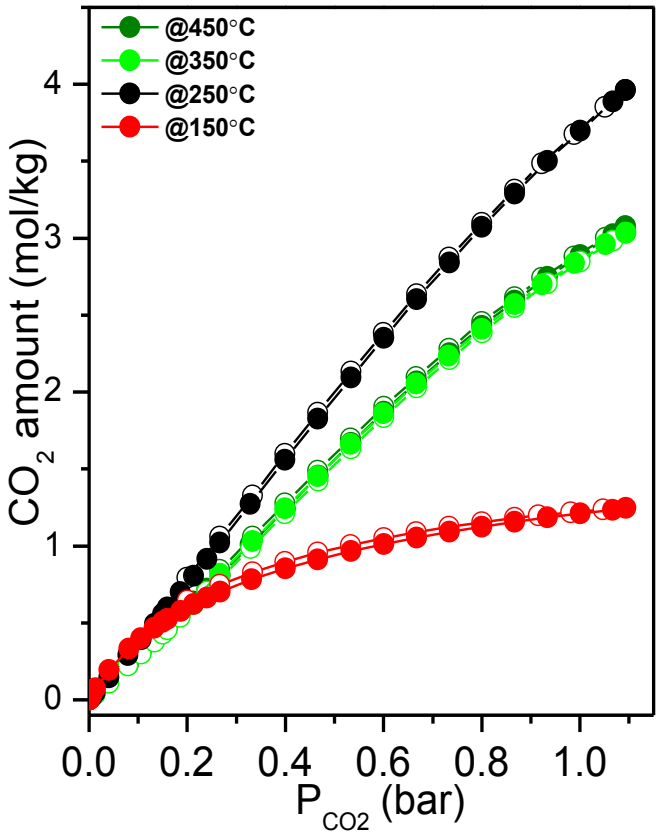

Figure S8. Excess CO_2 adsorption isotherms at 25°C obtained on Ce-BTC activated at 150°C (**MOF-76-Ce-hs**, red circles), 250°C (**MOF-76-Ce-ds**, black circles), 350°C (light green circles) and 450°C (olive green circles).

Table S4. Surface area and CO_2 adsorption capacity at 25°C and 1.1 bar.

Temperature (°C)	$S_{Langmuir}$ (m^2/g)	CO_2 amount (mol/kg)	CO_2 storage wt%
150	n.p.*	1.1	4.6
250	999	4.0	15
350	961	3.0	11.7
450	970	3.0	11.7

*n.p.: not porous

S10 *In situ* FT-IR Spectroscopy of CO_2 adsorption

FTIR spectroscopy has been also adopted to perform a preliminary study of CO_2 adsoprtion at 25°C on **MOF-76-Ce-ds sample,** obtained upon outgassing at 250°C in dynamic vacuum. (see Figure S9).

A maximum Peq(CO_2)=20 mbar was reached. Figure S8 shows an intense band centered at 2336 cm^{-1}, assigned to the asymmetric stretching mode (ν_3) of adsorbed CO_2. This mode is almost unperturbed with respect to the one reported for CO_2 in microporous matrix (2338 cm^{-1}). [4] Such a small perturbation of the CO_2 with respect to other open metal site MOFs as Mg-MOF-74 (2353 cm^{-1}) [5] indicate the lower availability to the interaction of Ce as expected because of its 6-coordination shell at the low pressure.

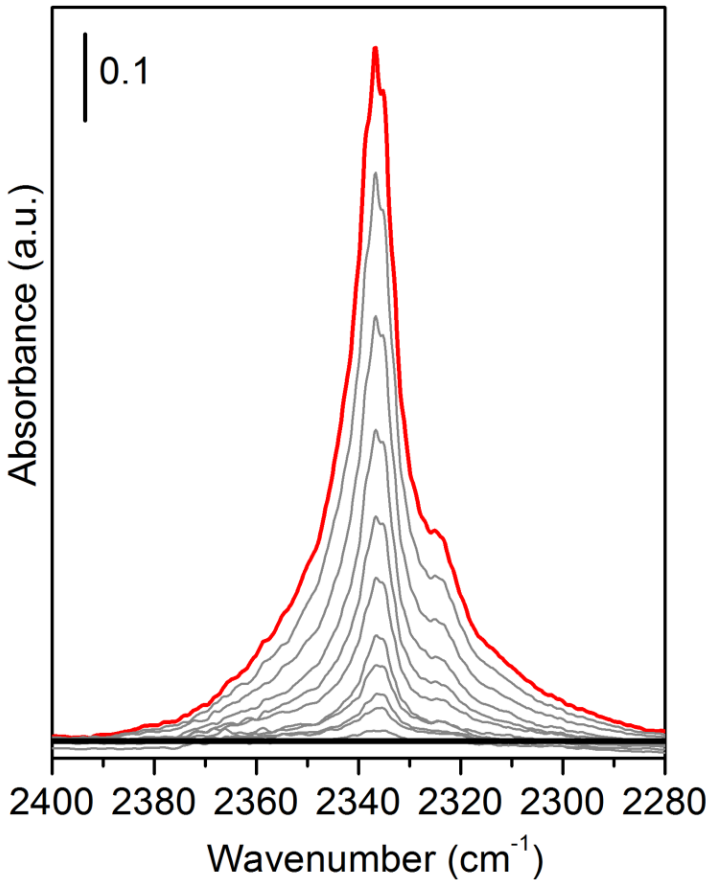

Figure S9. FTIR spectra of CO_2 adsorption on **MOF-76-Ce-ds** at RT. Red curve: 20 mbar CO_2 pressure; black curve: vacuum. Grey curves correspond to intermediate pressure values.

S11 Calorimetric CO_2 isotherms

This procedure allows for both the integral heats evolved (Q^{int}) and adsorbed amounts (n_{ads}) to be determined in the same experiment for very small increments of the adsorptive pressure. Adsorbed amounts and integral heats evolved, normalized to the surface area unit, were plotted versus pressure in the form of volumetric (quantitative) and calorimetric isotherms, respectively. The adsorption heats observed for each small dose of gas admitted over the sample (q_{diff}) were finally reported as a function of coverage to give the (differential) enthalpy changes associated with the proceeding adsorption process. The differential heat plots were obtained by taking the middle point of the partial molar heats ($\Delta Q^{int}/\Delta n_{ads}$, $kJmol^{-1}$) versus the n_{ads} histogram relative to the individual adsorptive doses.

For the sake of completeness, calorimetric CO_2 isotherms measured on Ce-BTC sample activated at 350°C are also reported (see Figure S10). They are almost coincident with those ones obtained on the sample activated at 250°C (**MOF-76-Ce-ds**).

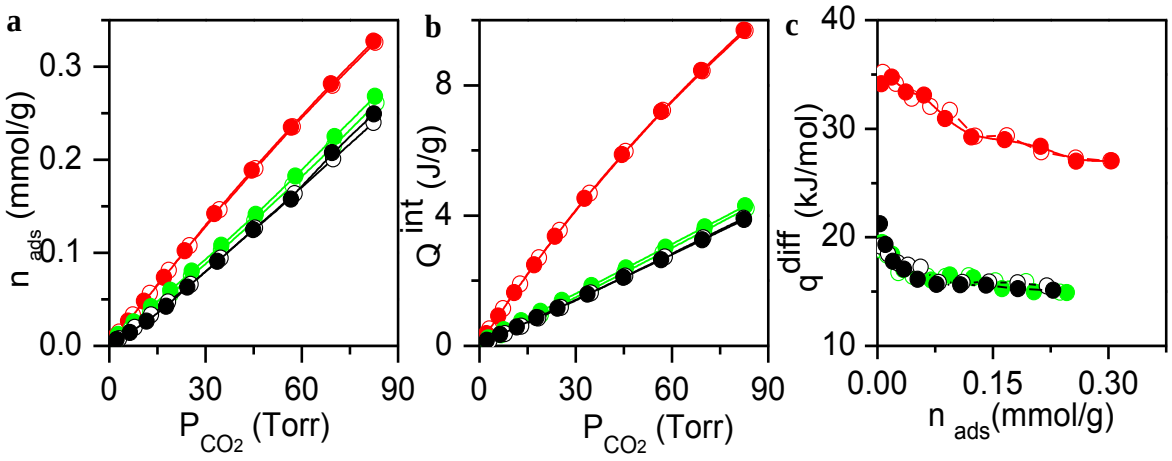

Figure S10. a) Volumetric isotherms. b) Calorimetric isotherms. c) Differential heat distribution obtained on **MOF-76-Ce** activated at 150°C (**MOF-76-Ce-hs**, red circles), 250°C (**MOF-76-Ce -ds**, black circles) and 350°C (light green circles). Empty and full squares indicates the primary and secondary isotherms obtained at each temperature of activation.

References

[1] C. Prestipino, L. Regli, J. G. Vitillo, F. Bonino, A. Damin, C. Lamberti, A. Zecchina, P. L. Solari, K. O. Kongshaug, S. Bordiga, *Chem. Mater.* **2006**, *18*, 1337-1346.

[2] *Materials Studio Version 5.0* **2009**, San Diego CA.

[3] a) E. Groppo, C. Prestipino, C. Lamberti, R. Carboni, F. Boscherini, P. Luches, S. Valeri, S. D'Addato, *Phys. Rev. B* **2004**, *70*, 165408; b) P. Luches, S. D'Addato, S. Valeri, E. Groppo, C. Prestipino, C. Lamberti, F. Boscherini, *Phys. Rev. B* **2004**, *69*, 045412; c) C. Lamberti, E. Groppo, C. Prestipino, S. Casassa, A. M. Ferrari, C. Pisani, C. Giovanardi, P. Luches, S. Valeri, F. Boscherini, *Phys. Rev. Lett.* **2003**, *91*, 046101; d) E. Groppo, C. Prestipino, C. Lamberti, P. Luches, C. Giovanardi, F. Boscherini, *J. Phys. Chem. B* **2003**, *107*, 4597-4606.

[4] J. G. Vitillo, M. Savonnet, G. Ricchiardi, S. Bordiga, *ChemSusChem* **2011**, *4*, 1281-1290.

[5] L. Valenzano, B. Civalleri, S. Chavan, G. T. Palomino, C. O. Arean, S. Bordiga, *J. Phys. Chem. C* **2010**, *114*, 11185-11191.